Ultrasonics Sonochemistry 92 (2023) 106271

Contents lists available at ScienceDirect

Ultrasonics Sonochemistry

journal homepage: www.elsevier.com/locate/ultson

Transition mechanisms of translational motions of bubbles in an ultrasonic field

Xiaojiao Wang [a], Zhi Ning [a,*], Ming Lv [a], Pengfei Wu [b,*], Chunhua Sun [a,c], Yechang Liu [a]

[a] Beijing Jiaotong Univ, Sch Mech Elect & Control Engn, Beijing 100044, China
[b] State Key Laboratory of Acoustics, Institute of Acoustics, Chinese Academy of Sciences, Beijing 100190, China
[c] Shanghai Marine Diesel Engine Research Institute, Shanghai, China

ARTICLE INFO

Keywords:
Ultrasonic cavitation
Translational motion
1/2 order subharmonic
Chaotic pair

ABSTRACT

The translation behaviors of oscillating bubbles are closely related to the polymerizations and dispersions between them, which are crucial for the ultrasonic cavitation effect. In this study, six types of translational motion of bubbles with a wide range of sizes (2–100 μm) in the R_{01}-R_{02} plane are investigated. Our results demonstrate that in addition (to the 2nd order harmonic), the 1/2 order subharmonic can change the bubble pairs from the three states of the attraction, stable after attraction, and repulsion to that of the repulsion, coalescence, and attraction, respectively. Furthermore, within the range of the main resonance radius and the 1/2 order subharmonic resonance radius, the chaotic bubble pairs with alternating attractive and repulsive forces appear in the region between the coalescence pairs and stable pairs after attraction. Finally, the corresponding physical mechanisms of the chaotic translational motions are also revealed.

1. Introduction

When an ultrasound propagates through an aqueous solution, the gas bubbles oscillate, expand and collapse, which is termed as acoustic cavitation [1,2]. The fluid flow effects (microjetting and shear force) and extreme environment (high temperature and pressure) caused by oscillation and collapse of bubbles [3,4] can be widely utilized in applications such as food processing [5], (heavy oil) viscosity reduction [6], cleaning [7], chemical reactions [8], ultrasonic welding [9], medical ultrasound (ultrasonic imaging and guide treatments) [10–16], among others. In addition, the translational motions of oscillating bubbles, triggered by primary and secondary Bjerknes forces [17,18], also have profound research and application significances. For instance, the polymerization and dispersion between bubbles caused by translational motion have a significant influence on the bubble cloud dynamics and cavitation effect [19–22]. Experimentations and numeric evaluations demonstrated that the packing of bubbles changes the attenuation of the bubbly medium [23]. Thus, a prediction of the translational motion of the bubbles and possible stable regions will also help to better understand the wave propagation in bubbly media. In this study, the dynamic behaviors of bubbles caused by secondary Bjerknes forces are emphasized and addressed.

According to the classical linear theory, if a driving frequency lies among the linear resonance frequencies, they will mutually attract; otherwise, they mutually repulse [17,24,25]. In the context of this linear theory, Zabolotskaya et al. [26] revealed that the secondary Bjerknes force transits from a state of mutual attraction to mutual repulsion as the inter-bubble distance decreases because the driving frequency falls between the increased linear resonance frequencies. This idea is reaffirmed while considering the multiple scattering of sound [27]. Furthermore, a similar sign inversion mechanism was discovered by Barbat [28] for near-resonant pairs of bubbles. Afterwards, Harkin [25] and Ida et al. [29,30] also confirmed that a change in the inter-bubble distance can lead to a sign change of the secondary Bjerknes force.

The sign reversal of the secondary Bjerknes force (or translational motion) owing to the nonlinear effect of bubble oscillations has attracted scientists [31–37]. Oguz et al. [31] indicated that even slight nonlinear oscillations of bubbles can change the sign of the secondary Bjerknes force predicted by the linear theory. Considering the non-spherical oscillations of coupled bubbles, Pelekasis et al. [32] revealed that the decreased distance in the inter-bubbles may reverse the direction of the secondary Bjerknes force. Although the non-spherical oscillations of only a small individual bubble was considered, Zhang et al. [33] concluded that the translational motions (inter-bubble distance) can significantly change the magnitude and sign of a bubble–bubble interaction.

In a strong ultrasonic field (>1.0 bar), sign reversal would also occur

* Corresponding authors.
E-mail addresses: zhining@bjtu.edu.cn (Z. Ning), wpf@mail.ioa.ac.cn (P. Wu).

https://doi.org/10.1016/j.ultsonch.2022.106271
Received 27 September 2022; Received in revised form 14 December 2022; Accepted 15 December 2022
Available online 17 December 2022

Nomenclature

C	sound velocity in liquid (m/s)
D	inter-bubble distance (μm)
D_0	initial inter-bubble distance (μm)
F_B	secondary Bjerknes force between two bubbles (N)
F_{ex1},F_{ex2}	Levich viscous drag acting on bubble 1 and bubble 2 (N)
F_{h1}	resultant external force acting on bubble 1 (N)
F	frequency of the sound field (kHz)
$f_{c\text{-}res1}$,$f_{c\text{-}res2}$	linear resonance frequencies of the coupled bubbles (kHz)
f_{nat1}, f_{nat2}	natural frequencies of the two individual bubbles (kHz)
f_{res1}, f_{res2}	linear resonance frequencies of the two individual bubbles (kHz)
f_{res}	linear resonance frequency of the individual bubble (kHz)
f_0	ultrasonic driving frequency (kHz)
F_{12}	radiation pressure acting on bubble 2 originated from bubble 1 (N)
$P_A(t)$	sinusoidal ultrasonic pressure (bar)
P_a	ultrasonic pressure amplitude (bar)
P_{s1}, P_{s2}	pressure emitted by the coupled pulsating bubbles (bar)
P_v	saturated vapor pressure (bar)
P_0	ambient atmospheric pressure (bar)
P_1, P_2	pressure at the walls of the coupled bubbles (bar)
R_{max1}, R_{max2}	maximum radii of the coupled bubbles (μm)
R_{res}	linear resonance radius corresponding to the driving frequency f_0 (μm)
R_1,R_2	instantaneous radii of the coupled bubbles (μm)
$\dot{R}_1$,$\dot{R}_2$	radial velocity of the coupled bubbles (μm/s)
$\ddot{R}_1$,$\ddot{R}_2$	radial acceleration of the coupled bubbles (μm/s^2)
R_{10}, R_{20}	equilibrium radius of the bubble 1 and bubble 2 (μm)
T	time (s)
T_0	driving period (s)
P	density of liquid medium (kg/m^3)
V_1, V_2	instantaneous volume of the coupled bubbles
v_1, v_2	liquid velocity generated by the coupled bubbles (μm/s)
x_1, x_2	translational displacements of the coupled bubbles (μm)
$\dot{x}_1$,$\dot{x}_2$	translational velocities of the coupled bubbles (μm/s)
$\ddot{x}_1$,$\ddot{x}_2$	translational accelerations of the coupled bubbles (μm/s^2)
M	viscosity of liquid medium (Pa·s)
κ	gas polytrophic exponent
σ	surface tension coefficient (N/m)

as the pressure amplitudes increase, as a result of the changes in the dynamical Blake threshold [18,34]. Using the Lagrangian formalism, Doinikov et al. [35] derived a model coupling the radial and translational motions to better understand the bubble dynamics, and reported that bubbles would form a steady pair instead of coalescing. Pelekasis and Doinikov et al. [34,36] revealed the relevant mechanism by which the 2nd order harmonic can prevent the bubbles from coalescing. Furthermore, Pelekasis summarized four types of translational motions. It was pointed out that the 1/2 subharmonic and combination resonances (unique resonance type for dual-frequency case) can affect the values and signs of the secondary Bjerknes force [37].

In addition, Zhang et al. [38] demonstrated that the translational motions not only lead to chaotic pulsations and secondary Bjerknes forces, but also improve the chaotic degree of secondary Bjerknes force. They also indicated that the repulsive secondary Bjerknes force is mainly due to the large radius catching the rebound point of another bubble [39]. Wang et al. [40] concluded that decreased frequency or increased burst ultrasound amplitude can increase the translational velocities.

However, despite the growing interest of the influences of nonlinear effect on the translational motions (or secondary Bjerknes force), the relative mechanisms caused by subharmonic waves remain obscure, especially those by chaotic dynamics that have not been reported yet. Therefore, in this study, a wide R_{01}-R_{02} space is scanned to investigate the distribution of the types of translational motions. Then, the transition mechanisms of the translational motions triggered by the 1/2 order subharmonic, and the translational and radial motion characteristics of chaotic pairs are analyzed. Finally, the influence of the initial inter-bubble distance and driving frequency on the translational motions are analyzed.

2. Model and solutions

2.1. Dynamic model

Two coupled bubbles were assumed to be located sufficiently distant compared to their radii. The influence of higher-order spherical harmonics of surface modes was neglected and the bubble oscillations were considered completely spherically symmetric [41,42]. In particular, the subharmonic emissions were experimentally demonstrated to be affected by non-spherical oscillations [42]. Thus, the influences of the surface modes were neglected for simplification of the study. The time delay effect of sound wave propagation owing to the inter-bubble distance was ignored in this study. The study conducted by the Hamilton et al. [43–46] regarding the time delay effects can be referred for further details. The possible influence of time delays on the dynamic behaviors of the interacting bubbles are reviewed in Ref. [47]. The bubble oscillations were considered to be stable and the destruction threshold was neglected. In many scenarios of high amplitude oscillations where $R/R_0 > 2$, a bubble may be unable to stably oscillate for several cycles [48]. This appears to be the minimum threshold for inertial bubble collapse and possible destruction [49]. In addition, this present study did not account for the mass transfer effects, which are important at a higher number of cycles, such as those studied in reference [50]. Similar to the previous studies regarding the dynamic behavior of interacting bubbles, the effect of mass transfer was neglected in this study.

Fig. 1 provides the schematic diagram of the dynamic interactions between the two coupled bubbles. R_{01} and R_{02} are the equilibrium radii of bubble 1 and bubble 2, respectively.

The pressure emitted by the adjacent pulsating bubbles can be calculated as follows [18]:

$$p_{s1} = \frac{\rho}{D}\frac{\mathrm{d}}{\mathrm{d}t}\left(R_2^2\dot{R}_2\right) \tag{1}$$

$$p_{s2} = \frac{\rho}{D}\frac{\mathrm{d}}{\mathrm{d}t}\left(R_1^2\dot{R}_1\right) \tag{2}$$

where P_{s1} is the pressure emitted by pulsating bubble 2 acting on bubble 1, and P_{s2} is the pressure emitted by pulsating bubble 1 acting on

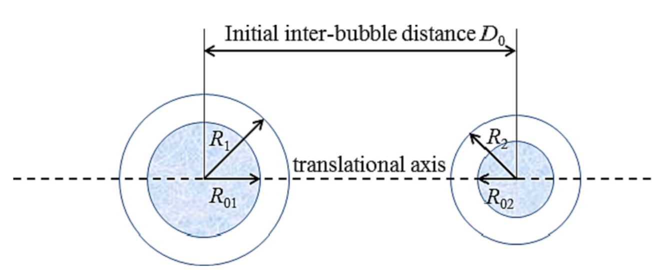

Fig. 1. Schematic diagram of the two coupled bubbles system.

bubble 2. R_1 and R_2 are the instantaneous radii of the coupled bubbles, and $\dot{R}_1$ and $\dot{R}_2$ are the radial velocities of the coupled bubbles. ρ is the density of the liquid medium, D denotes the inter-bubble distance.

The radiation pressure F_{12} acting on bubble 2, which originates from the oscillating bubble 1, can be expressed as follows:

$$F12 = -V_2 \nabla p_{s1} \tag{3}$$

With the volume of bubble 2:

$$V_2 = 4\pi R_2^3/3 \tag{4}$$

Substituting Eqs. (1–4) into Eq. (3) obtains followings:

$$F_{12} = -V_2 \frac{\partial p_{s1}}{\partial D} = V_2 \frac{\rho}{D^2}\frac{d}{dt}\left(R_1^2 \dot{R}_1\right) = \frac{\rho}{4\pi D^2} V_2 \frac{d^2 V_1}{dt^2} \tag{5}$$

By the integration of Eq. (5) within one period of bubble oscillation, the secondary Bjerknes force F_B can be obtained as follows:

$$F_B = \langle F_{12} \rangle = -\frac{\rho}{4\pi D^2}\left\langle \dot{V}_1 \dot{V}_2 \right\rangle \tag{6}$$

Here, $\dot{V}_1 = 4\pi R_1^2 \dot{R}_1, \dot{V}_2 = 4\pi R_2^2 \dot{R}_2$. The positive F_B indicates that the bubbles are mutually repulsive, while the negative F_B indicates that the two bubbles are mutually attractive.

In this study, a model derived by Doinikov [35] based on the Keller-Miksis equations [51] are employed to describes the coupled pulsations and translational motions of bubbles

$$\begin{gathered}\left(1-\frac{\dot{R}_1}{c}\right)R_1\ddot{R}_1 + \dot{R}_1^2\left(\frac{3}{2}-\frac{\dot{R}_1}{2c}\right) - \frac{P_1}{\rho}\left(1+\frac{\dot{R}_1}{c}\right) - \frac{R_1}{\rho c}\frac{dP_1}{dt} \\ = \frac{\dot{x}_1^2}{4} - \frac{R_2^2\ddot{R}_2 + 2R_2\dot{R}_2^2}{D} + \frac{R_2^2(\dot{x}_1\dot{R}_2 + R_2\ddot{x}_2 + 5\dot{R}_2\dot{x}_2)}{2D^2} - \frac{R_2^3\dot{x}_2(\dot{x}_1 + 2\dot{x}_2)}{2D^3}\end{gathered} \tag{7}$$

$$\begin{gathered}\left(1-\frac{\dot{R}_2}{c}\right)R_2\ddot{R}_2 + \dot{R}_2^2\left(\frac{3}{2}-\frac{\dot{R}_2}{2c}\right) - \frac{P_2}{\rho}\left(1+\frac{\dot{R}_2}{c}\right) - \frac{R_2}{\rho c}\frac{dP_2}{dt} \\ = \frac{\dot{x}_2^2}{4} - \frac{R_1^2\ddot{R}_1 + 2R_1\dot{R}_1^2}{D} - \frac{R_1^2(\dot{x}_2\dot{R}_1 + R_1\ddot{x}_1 + 5\dot{R}_1\dot{x}_1)}{2D^2} - \frac{R_1^3\dot{x}_1(\dot{x}_2 + 2\dot{x}_1)}{2D^3}\end{gathered} \tag{8}$$

$$\frac{R_1\ddot{x}_1}{3} + \dot{R}_1\dot{x}_1 + \frac{1}{D^2}\frac{d}{dt}(R_1R_2^2\dot{R}_2) - \frac{R_2^2(R_1R_2\ddot{x}_2 + R_2\dot{R}_1\dot{x}_2 + 5R_1\dot{R}_2\dot{x}_2)}{D^3} = \frac{F_{ex1}}{2\pi\rho R_1^2} \tag{9}$$

$$\frac{R_2\ddot{x}_2}{3} + \dot{R}_2\dot{x}_2 - \frac{1}{D^2}\frac{d}{dt}(R_2R_1^2\dot{R}_1) - \frac{R_1^2(R_2R_1\ddot{x}_1 + R_1\dot{R}_2\dot{x}_1 + 5R_2\dot{R}_1\dot{x}_1)}{D^3} = \frac{F_{ex2}}{2\pi\rho R_2^2} \tag{10}$$

Here, $\ddot{R}_1$ and $\ddot{R}_2$ are the radial accelerations of the coupled bubbles. x_1 and x_2 are the translational displacements of the coupled bubbles 1 and 2, $\dot{x}_1$ and $\dot{x}_2$ are the translational velocities of the coupled bubbles, and $\ddot{x}_1$ and $\ddot{x}_2$ are translational accelerations of bubbles 1 and 2. c is the sound velocity in liquid, P_v denotes the vapor pressure, P_0 denotes the atmospheric static pressure, κ is the polytrophic exponent, σ is the surface tension coefficient, and μ is the liquid viscosity. P_1 and P_2 denote the pressures at the bubble walls, which can be expressed as follows:

$$P_1 = \left(P_0 - P_v + \frac{2\sigma}{R_{10}}\right)\left(\frac{R_{10}}{R_1}\right)^{3\kappa} + P_v - \frac{2\sigma}{R_1} - \frac{4\mu\dot{R}_1}{R_1} - P_0 - P_A(t) \tag{11}$$

$$P_2 = \left(P_0 - P_v + \frac{2\sigma}{R_{20}}\right)\left(\frac{R_{20}}{R_2}\right)^{3\kappa} + P_v - \frac{2\sigma}{R_2} - \frac{4\mu\dot{R}_2}{R_2} - P_0 - P_A(t) \tag{12}$$

Where $P_A(t)$ denotes the sinusoidal ultrasonic pressure

$$P_A(t) = P_a \sin(2\pi f_0 t) \tag{13}$$

The external forces F_{axi} acting on bubble i are equal to the Levich viscous drag [52] and given by the followings:

$$F_{ex1} = -12\pi\mu R_1(\dot{x}_1 - \nu_2) \tag{14}$$

$$F_{ex2} = -12\pi\mu R_2(\dot{x}_2 - \nu_1) \tag{15}$$

Here, ν_i is the liquid velocity generated by bubble i and can be expressed as follows:

$$\nu_1 = \frac{R_1^2\dot{R}_1}{D^2} + \frac{R_1^3\dot{x}_1}{D^3} \tag{16}$$

$$\nu_2 = -\frac{R_2^2\dot{R}_2}{D^2} + \frac{R_2^3\dot{x}_2}{D^3} \tag{17}$$

The 4–5 order Runge-Kutta integration method is used to solve this coupled dynamic model (Eqs. (7–10)). The parametric values of the liquid medium are as follows: $\mu = 0.001$ Pa·s, $\sigma = 0.0728$ N/m, $c = 1500$ m/s, $\kappa = 4/3$, $\rho = 998$ kg/m^3, $P_v = 0.0233$ bar, and $P_0 = 1$ bar.

For a spherical bubble in infinite medium, without considering the interaction between the bubbles varying with the inter-bubble distance [10,23,47,53], the natural frequency for its volume oscillations f_{nat} for Keller-Miksis model reads as follows [54]:

$$f_{nat} = \frac{1}{2\pi R_0}\sqrt{\frac{3\kappa\left(P_0 + \frac{2\sigma}{R_0} - P_v\right) - \frac{2\sigma}{R_0} - \frac{4\mu^2}{\rho R_0^2}}{\rho}} \tag{18}$$

When the value of P_a is low, the value of the linear resonance frequency f_{res} of the individual bubble is approximately equal to that of its natural frequency f_{nat}. Fig. 2 provides the frequency response curves of an individual bubble when the pressure amplitudes are as follows: P_a = 0.005, 0.1, 0.3, 0.6 and 0.9 bar. According to Lauterborn [55], when the frequency of the sound field f is close to a rational number "m/n" (m, n = 1, 2, 3,…) times the linear resonance frequency f_{res}, all the resonances in Fig. 2 can be classified into four types according to the "order" (the inverse of "m/n"):

i) Main resonance (1/1): around $f / f_{res} = 1$;
ii) Harmonics resonance (2/1, 3/1, 4/1,…): around f / f_{res} = 1/2, 1/3, 1/4,….
iii) Subharmonic resonance (1/2, 1/3, 1/4,…): around f / f_{res} = 2, 3, 4,…….
iv) Ultraharmonic resonance (3/2, 5/2, 7/2,…): around f / f_{res} = 2/3, 2/5, 2/7,… ($m < n$).

Fig. 2 demonstrated that with P_a increasing, all resonances lean towards the lower frequencies [10,23,47,56,57]. Furthermore, the detailed work on the comprehensive oscillation characteristics of the 2nd and 3rd order harmonically resonant bubbles could be referred to Ref. [58]. By a novel method [59], Sojahrood et al. comprehensively characterized the evolution of 2nd, 3rd harmonic and subharmonics as a function of pressure [60]. The onset of the first subharmonic (1/2 order) resonance was proposed as a method to determine the cavitation

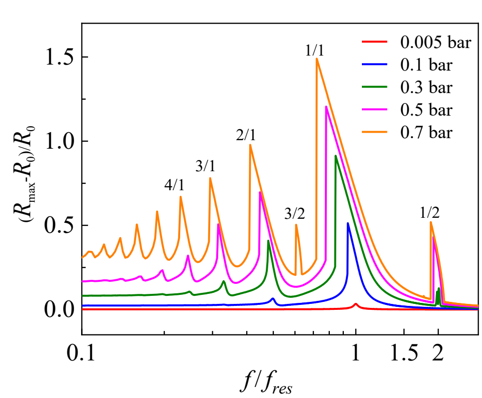

Fig. 2. Frequency response curves of the individual bubble when P_a = 0.005, 0.1, 0.3, 0.5 and 0.7 bar. R_0 = 10 μm. The numbers labelled above the peaks of the curves are the orders of resonances.

threshold [55]. One of the main applications of the 1/2 order subharmonic emissions is in the medical ultrasound. In imaging applications, they are used to enhance the detection of blood vessels with superior contrast in real-time [10–16]. Noted, ultraharmonics can also be used for ultrasonic imaging [61]. In therapy, 1/2 order subharmonics are used to monitor and guide treatments [10–16]. The pulses in therapy are long; and the conditions for the generation, amplification or disappearance of the 1/2 order subharmonic will help optimize and understand the treatment process.

The generation of 1/2 order subharmonics from spherical bubble oscillations was recently comprehensively studied [10,47,49,62–66]. The 1/2 order subharmonic emissions can be generated when the bubble is sonicated at its resonance [49,66], and the 1/2 order subharmonic emissions can be generated at twice the resonance frequency at the lowest acoustic pressure [10,47,49,64,65]. However, when full thermal dissipation was considered, the lowest pressure threshold occurred when the bubble was sonicated at a frequency below its resonance (sonication with the 3/2 or 5/2 order subharmonic resonance) [66]. Sojahrood et al. [49] indicated that when the bubble was sonicated at its resonance frequency, the 1/2 order subharmonic resonance is mainly generated when $R/R_0 > 2$ and during violent collapses.

2.2. Solution procedure

The dynamic behaviors of two-bubble system are mainly affected by the pressure amplitude and driving frequency of the ultrasonic wave, initial inter-bubble distance, and equilibrium radii of bubbles. In this study, if not indicated otherwise, the liquid physical parameters remain unchanged. The secondary Bjerknes forces within a pressure amplitude range of 0.005–0.9 bar are examined. In this manner, full considerations of the influences of the resonance effect (main, harmonic, and subharmonic resonances) are presented. To ensure that the dynamic behaviors of the two bubbles have reached a stable state, 15,000 periods of driving frequencies were employed for each calculation; 50 × 50 (the step size is 2 μm) calculations were performed in each R_{10}-R_{20} plane. The initial inter-bubble distance was set as 1500–7500 μm, which is significantly larger than the equilibrium radii of bubbles. The parameter values and ranges employed in this study are summarized in Table 1.

3. Results and discussion

The translational motions are mainly governed by the interaction force between the bubbles. Therefore, we first examine the case when R_{01} is invariant ($R_{01} = 10$ and 44 μm), the variations of F_B with R_{02}, as shown in Fig. 3. The linear resonance radius R_{res} (≈ 45 μm) corresponding to the driving frequency ($f_0 = 75$ kHz) is marked with an arrow on the coordinate. The positive F_B indicates that the bubbles are mutually repulsive, while the negative F_B indicates that the two bubbles are mutually attractive.

Fig. 3 shows that the F_B reaches a maximum at $R_{02} \approx R_{res}$, which indicates that the strongest attraction and repulsion forces are generated when the bubble performs its main resonance. If the driving frequency f_0 lies between f_{res1} and f_{res2}, ($R_{01} < R_{res} < R_{02}$; $R_{02} < R_{res} < R_{01}$), the bubbles repulse each other; otherwise ($R_{res} < R_{01}$ and $R_{res} < R_{02}$; $R_{01} < R_{res}$ and $R_{02} < R_{res}$), they attract each other [17,24,25]. Therefore, in Fig. 3(a), the direction of F_B transits from negative to positive at $R_{02} > R_{res}$, while transits from positive to negative values at the same range in Fig. 3(b). With P_a increasing, the presence of the 2nd and 3rd order harmonics (resonance radii corresponding to $2f_0$ and $3f_0$) triggers the sign reversal of F_B, whereas the 1/2 order subharmonic (resonance radius corresponding to $1/2f_0$) only significantly enhances F_B instead of reversing its sign. In addition, the position of the resonance radii corresponding to the main, 2nd (3rd), and 1/2 order resonance frequencies of the coupled bubbles gradually moves towards the left with P_a increasing, which is also reflected in the R_{01}-R_{02} planes in the following sections. This owing to the fact that all the resonance frequencies lean towards lower frequencies due to the "bending phenomenon" in nonlinear dynamics as the P_a increases [37,55].

Table 1
The parameter settings for a two-bubble system.

Parameters	Range
Pressure amplitude P_a/bar	0.005/0.1/0.3/0.6/0.9
Driven frequency f_0/kHz	45/75/105/135
Initial inter-bubble distance D_0/μm	1500/3500/5500/7500
Equilibrium radius of bubble 1 R_{01}/μm	2–100
Equilibrium radius of bubble 2 R_{02}/μm	2–100

Fig. 4 provides the schematic diagram of six types of translational motions of bubbles under the action of F_B: (a) pair with invariant inter-bubble distance, (b) stable pair after attraction, (c) coalescence pair after mutual attraction, (d) stable pair after mutual repulsion, (e) constantly repulsive pair, and (f) chaotic pair. It should be explained that the invariant inter-bubble distance refers to the variation of inter-bubble distance within 15,000 periods of driving frequency is within the initial inter-bubble distance of 10^{-4}, so it can be ignored.

A large range of equilibrium radii of the bubbles was employed to study the translational motions when P_a was 0.1, 0.3, 0.6, and 0.9 bar, as shown in Fig. 5. f_0 and D_0 are 75 kHz and 3500 μm. As shown in Fig. 5(a), for $P_a = 0.1$ bar, there are four regions divided by R_{res} in the R_{01}-R_{02} plane [37]:

I Attractive regions ($F_B < 0$): $R_{res} > R_{01}$ and $R_{res} > R_{02}$; $R_{res} < R_{01}$ and $R_{res} < R_{02}$;
II Repulsive regions ($F_B > 0$): $R_{01} < R_{res} < R_{02}$; $R_{01} < R_{res} < R_{02}$.

As shown in Fig. 5, all distributed regions are characterized by a diagonal symmetry. Most of the green region is located at the left bottom corner of the R_{10}-R_{20} plane. This is because when R_{01} and/or R_{02} are small, their radial oscillations are significantly weak, resulting in the nearly negligible translational displacements under low F_B values. As P_a increases, the green region is slightly constricted, which can be explained by the apparent translational velocities caused by the stronger radial oscillations because the translational motions follow the radial oscillations [34].

Additionally, the coalescence bubble pairs are mainly concentrated in two regions: 1) where R_{01} and R_{02} are similar (near the diagonal), and 2) where the main, 2nd (3rd, 4th) order harmonics (dotted black circles) and 1/2 order subharmonic (dotted red circles) appear, and the sharply increased F_B causes the bubbles to coalesce. As P_a increases, the 2nd (3rd, 4th) order harmonics and 1/2 order subharmonic led to a sign reversal of the translational motions, which will be further explained. Note, between the region signifying coalescence pair and stable pair after attraction, the chaotic pair (yellow region) with an alternate attraction and repulsion force can be observed.

For large amplitude of acoustic pressure, the strong-nonlinear oscillations make the phases of the bubble oscillations highly uncertain. The collapse and rebound stages of the bubble oscillations lead to a complex and changeable phase relationship between the two bubbles. In particular, when the pressure amplitude is greater than the dynamic Blake threshold ($P_a \approx 1.3$ bar), the nonlinear effects of the bubble oscillations are significantly apparent, which causes the difference between the linear resonance frequency and natural frequency of the bubble to be very large. Therefore, it may not be appropriate to divide the different regions of the secondary Bjerknes force (or transitional motions) by the linear resonance radius.

3.1. Transitions of the translation motions of the bubbles

Six pairs of bubbles, indicated by filled circles in Fig. 5(b), are selected to explore the transformation mechanism of the translational motions triggered by the 2nd order harmonic, 1/2 order subharmonic,

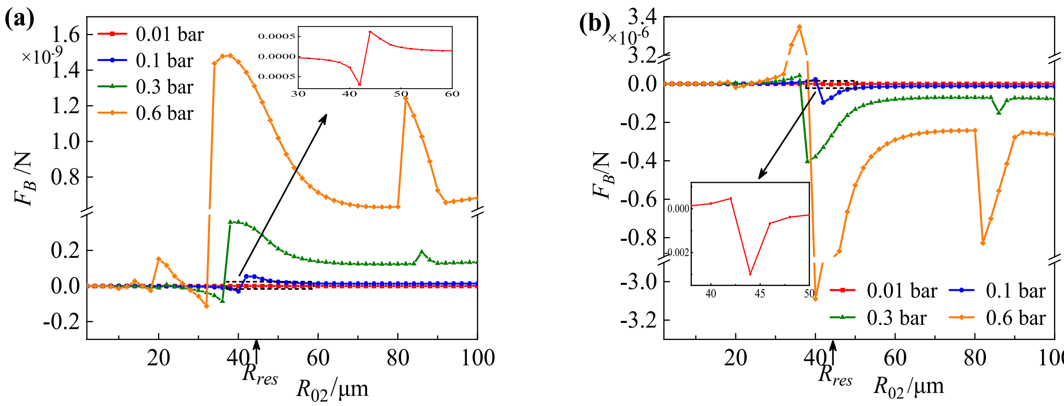

Fig. 3. The variation of the secondary Bjerknes force F_B with R_{02}. **(a)** $R_{01} = 10$ μm; **(b)** $R_{01} = 44$ μm. P_a is 0.01, 0.1, 0.3, and 0.6 bar. $f_0 = 75$ kHz and $D_0 = 3500$ μm. R_{res}: linear resonance radius corresponding to the driving frequency f_0.

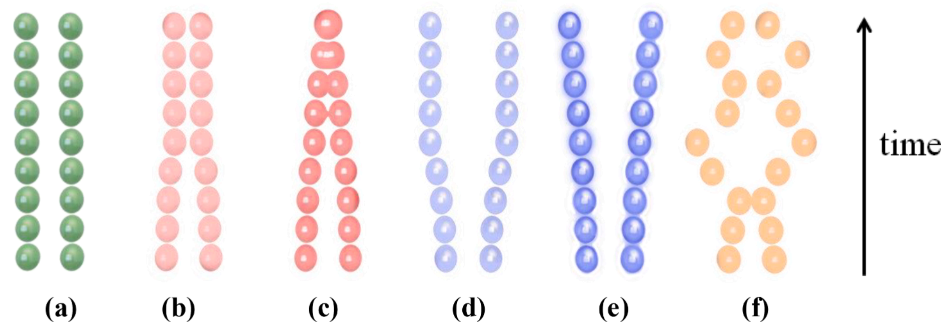

Fig. 4. Schematic diagram of the six types of translational motions.

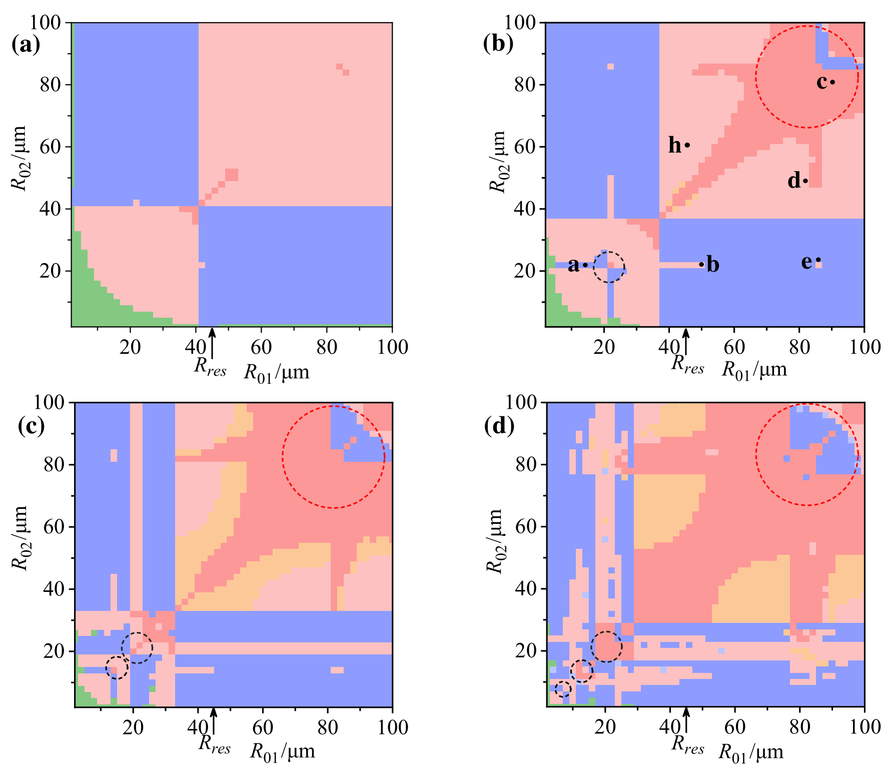

Fig. 5. The R01-R02 plane distribution diagram for the six types of translational motions. (a) Pa = 0.1 bar, (b) Pa = 0.3 bar, (c) Pa = 0.6 bar, and **(d)** $P_a = 0.9$ bar respectively. $f_0 = 75$ kHz and $D_0 = 3500$ μm. Different regions are: constantly repulsion pair; stable pair after repulsion; pair with invariant inter-bubble distance, stable pair after mutual attraction; coalescence pair after mutual attraction, chaotic pair.

and chaos. For point **a** (R_{01} = 14 & R_{02} = 22 μm), the effect of the 2nd order harmonic increases as P_a increases, which leads to the aggregated bubbles becoming repulsive [34]. Fig. 6 presents the time-dependent inter-bubble distance of four bubble pairs (point **b**, **c**, **d** and **e**) when P_a = 0.1, 0.3, 0.6, and 0.9 bar. The translational motions shift from attraction to repulsion or vice versa as P_a increases, indicating that the behavior of bubbles is closely related to P_a. Note, when P_a = 0.1 bar, the translational motions have not reached a stable state within the limited periods; however, they are the candidates for the formation of stable pairs after attraction because significantly longer time is required for the viscous drag force to decelerate the translational velocity and reach a the steady state [34].

Fig. 7 presents the noise spectra of the radial variations of the bubbles (R_{01} = 50 μm, R_{02} = 22 μm) over time and the frequency response curves of the two bubbles when P_a = 0.005 bar (linear condition). Note, when P_a is low and the interaction force between the bubbles is ignored, the values of the linear resonance frequencies of the individual bubble (f_{res1} and f_{res2}) are approximately equal to that of their natural frequencies (f_{nat1} = 65 kHz and f_{nat2} = 149 kHz). In this case (the inter-bubble distance is significantly larger that their radii), the values of linear resonance frequencies of the coupled bubbles ($f_{c\text{-}res1}$ and $f_{c\text{-}res2}$) are also approximately equal to that of f_{nat1} and f_{nat2}. When P_a = 0.1 bar, $f_{c\text{-}res1}$ (=65 kHz) and $f_{c\text{-}res2}$ (=149 kHz) are located at the two sides of the frequency of the sound field f (=f_0 = 75 kHz) (Fig. 7(c)), leading to the mutually repulsive translational motions because the F_B caused by the out-of-phase radial oscillations is repulsive. When P_a = 0.3, 0.6 and 0.9 bar, the 2nd order harmonic (2f_0 = 150 kHz) is increasingly pronounced (Fig. 6(b)). $f_{c\text{-}res1}$ (=65 kHz) and $f_{c\text{-}res2}$ (=149 kHz) are located at the left side of f (=150 kHz) (Fig. 7(c)), which causes the bubbles to oscillate in phase and finally inverts the translational motions from repulsion to attraction.

Similarly, the noise spectra of radial variations of the bubbles (R_{01} = 90 μm, R_{02} = 82 μm) over time (Fig. 6(b)) and the frequency response curves are also examined in Fig. 8. When P_a = 0.1 or 0.3 bar, the fundamental frequency (f_0 = 75 kHz) is the most predominant among the frequency domain (Fig. 7(a) and (b)). The frequency of the sound field f (=f_0) is greater than $f_{c\text{-}res1}$ (=36 kHz) and $f_{c\text{-}res2}$ (=40 kHz) (Fig. 8 (c)), which leads to the mutually attractive translational motions caused by the in-phase radial oscillations. When P_a = 0.6 or 0.9 bar, the 1/2 order subharmonic (1/2f_0 = 37.5 kHz) dominates the noise spectra (Fig. 8(a) and (b)). The frequency of the sound field f (=1/2f_0) falls between $f_{c\text{-}res1}$ and $f_{c\text{-}res2}$ (Fig. 8(c)), which indicates that the bubbles would repel each other.

Fig. 9 further illustrates the variations in the radial oscillations of the bubbles (R_{01} = 90 & R_{02} = 82 μm) and the secondary Bjerknes force F_B over the normalization driving period. When P_a = 0.1 or 0.3 bar, the radial oscillation period is equal to the driving period T_0, and F_B is always negative (attraction force) because the phases of the radial oscillations of the two bubbles are synchronized in real-time (Fig. 9(a) and (b)). When P_a = 0.6 or 0.9 bar, the radial oscillations of the bubbles with a period of 2 T_0 indicates that the 1/2 order subharmonic resonance has occurred. The time-averaged F_B in one driving period is positive (repulsion force) because the out-of-phase radial oscillations of the two bubbles are dominant (Fig. 9(c) and (d)).

Meanwhile, the time-dependent radial oscillations of the bubbles (R_{01} = 82 & R_{02} = 48 μm) and F_B are also illustrated in Fig. 10. When P_a = 0.1 or 0.3 bar, F_B is always negative (attraction force) owing to the real-time in-phase radial oscillations of the two coupled bubbles (Fig. 10 (a) and (b)). When P_a = 0.6 or 0.9 bar, the period of radial oscillation for bubble 2 (blue curves) is equal to T_0, while that of bubble 1 (red curves) is twice as the value of T_0. Despite the aforementioned, the time-averaged F_B in one driving period remains negative (attraction force) because the in-phase radial oscillations are dominant in every driving period (Fig. 10(c) and (d)). Furthermore, the significantly increased F_B caused by the large oscillation amplitudes would result in the polymerization of bubbles (Fig. 6(c)). Note, when P_a = 0.9 bar, the radial oscillation amplitudes are greater than those of P_a = 0.6 bar, which makes the bubbles coalesce within a shorter time than that of P_a = 0.6 bar (Fig. 6(c)). Because the transition mechanisms of the translational motions of bubbles with R_{01} = 86 & R_{02} = 24 μm (Fig. 6 (d)) are similar to those shown in Fig. 6(a-c), they are not repeatedly explained.

Fig. 5 shows that the chaotic bubble pair primarily appears between the regions signifying the coalescence pair and stable distance after attraction. For a better understanding, Fig. 11 examines the time

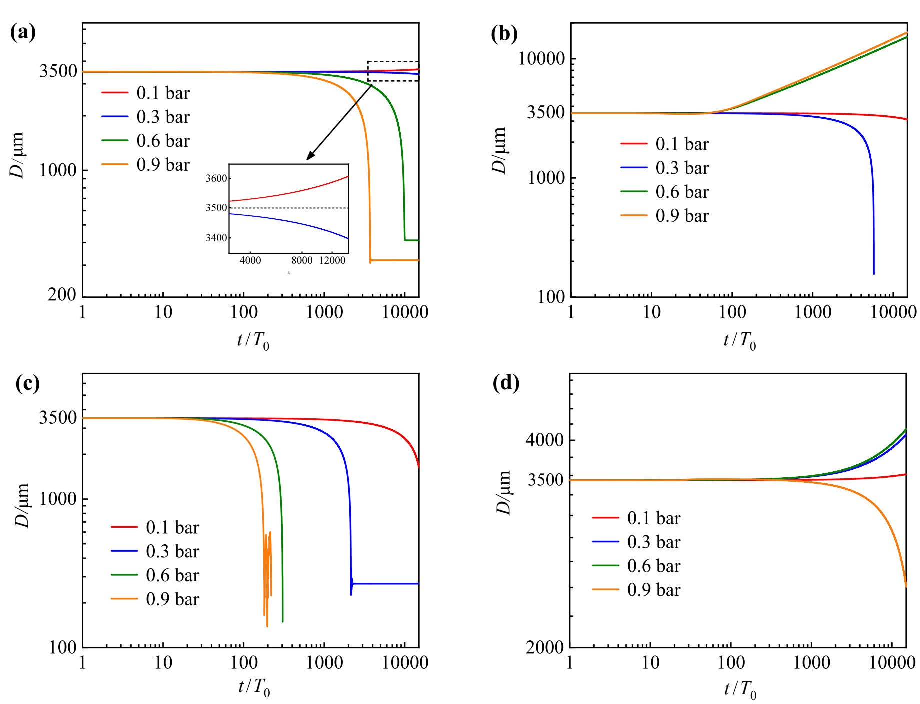

Fig. 6. Variation in the inter-bubble distance of bubble pairs with R_{01} and R_{02} **(a)** 50 & 22 μm (point **b**), **(b)** 90 & 82 μm (point **c**), **(c)** 82 & 48 μm (point **d**), and **(d)** 86 & 24 μm (point **e**) with normalized periods. P_a = 0.1, 0.3, 0.6, and 0.9 bar, f_0 = 75 kHz and D_0 = 3500 μm.

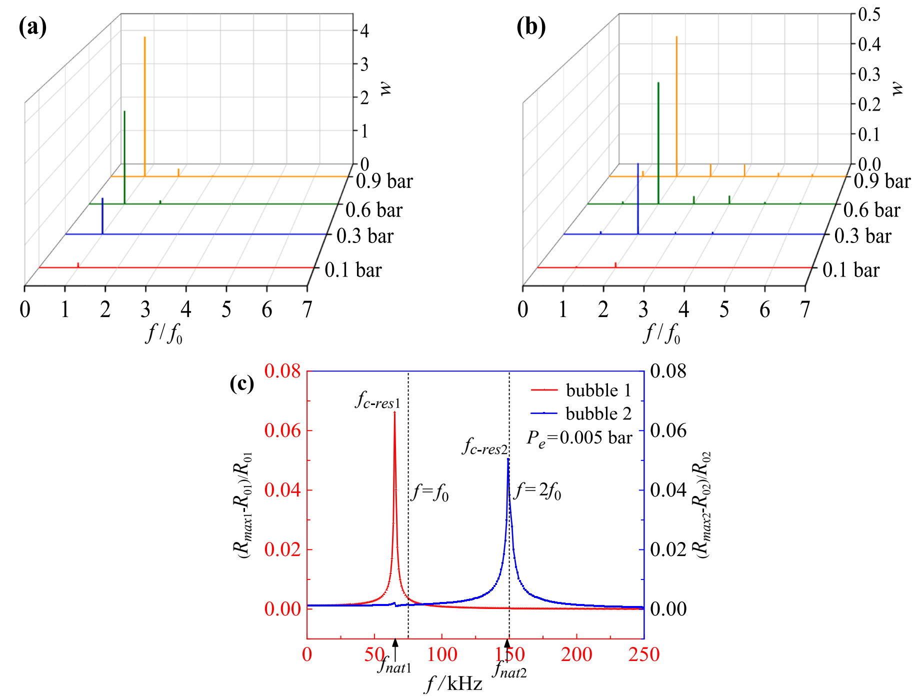

Fig. 7. Noise spectra of the radial variations over time: **(a)** bubble 1, R_{01} = 50 μm; **(b)** bubble 2, R_{02} = 22 μm when P_a = 0.1, 0.3, 0.6, and 0.9 bar; and **(c)** frequency response curves of the two bubbles when P_a = 0.005 bar. D_0 = 3500 μm. f_0: (=75 kHz), ultrasonic driving frequency (fundamental frequency). $2f_0$: (=150 kHz), 2nd order harmonic frequency. f: frequency. R_{max1} and R_{max2}: maximum radii of the coupled bubbles. $f_{c\text{-}res1}$ and $f_{c\text{-}res2}$: linear resonance frequencies of the coupled bubbles. f_{nat1} and f_{nat2}: natural frequencies of the two individual bubbles.

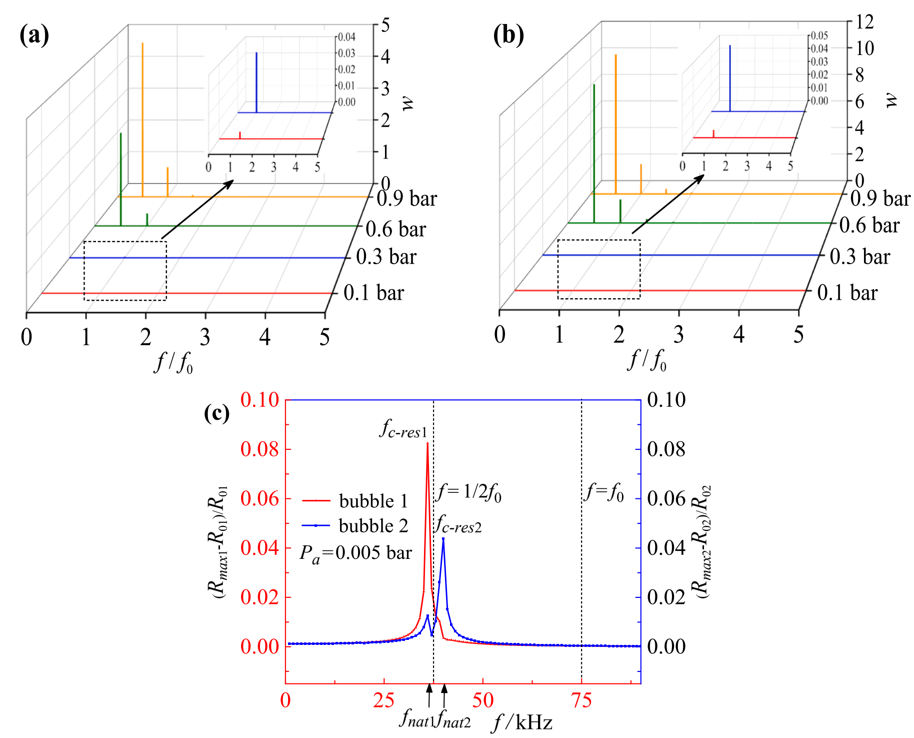

Fig. 8. Noise spectra of the radial variations over time: **(a)** bubble 1, R_{01} = 90 μm; **(b)** bubble 2, R_{02} = 82 μm, when P_a = 0.1, 0.3, 0.6, and 0.9 bar and **(c)** the frequency response curves of the two bubbles when P_a = 0.005 bar. D_0 = 3500 μm. f_0 = 75 kHz and D_0 = 3500 μm. f_0: (=75 kHz), ultrasonic excitation frequency (fundamental frequency). $1/2f_0$: 1/2 order subharmonic frequency. f: frequency. R_{max1} and R_{max2}: maximum radii of the coupled bubbles. $f_{c\text{-}res1}$ and $f_{c\text{-}res2}$: linear resonance frequencies of the coupled bubbles. f_{nat1} and f_{nat2}: natural frequencies of the two individual bubbles.

evolution of the translational displacements of the bubbles (R_{01} = 46 μm, R_{02} = 60 μm) when P_a is 0.1, 0.3, 0.6, and 0.9. When P_a = 0.1 or 0.3 bar, the bubbles constantly attract each one another until an invariable D is reached (Fig. 11 (a) and (b)). However, when P_a = 0.3 bar, the time required to reach a steady state is reduced compared to that of P_a = 0.1 bar. For P_a = 0.6 bar, the translational motions are characterized by the alternate motions of attraction and repulsion (Fig. 11 (c)). For P_a = 0.9 bar, the chaotic translational motions are more violent, and the bubbles eventually coalesce at a certain moment (Fig. 11 (d)).

The inter-bubble distances over time are processed based on the Fast-Fourier-transform method, and the corresponding amplitude-frequency curves are presented in Fig. 12. As P_a increases, the noise amplitudes of the translational motions increase in entirety. When P_a = 0.1 bar, only the fundamental ($f = f_0$) and harmonic spectral lines ($f = 2f_0$, $3f_0$, $4f_0$, $5f_0$) appear in the spectrum. When P_a = 0.3 bar, in addition to the fundamental and harmonic spectral lines, the broadband noises first

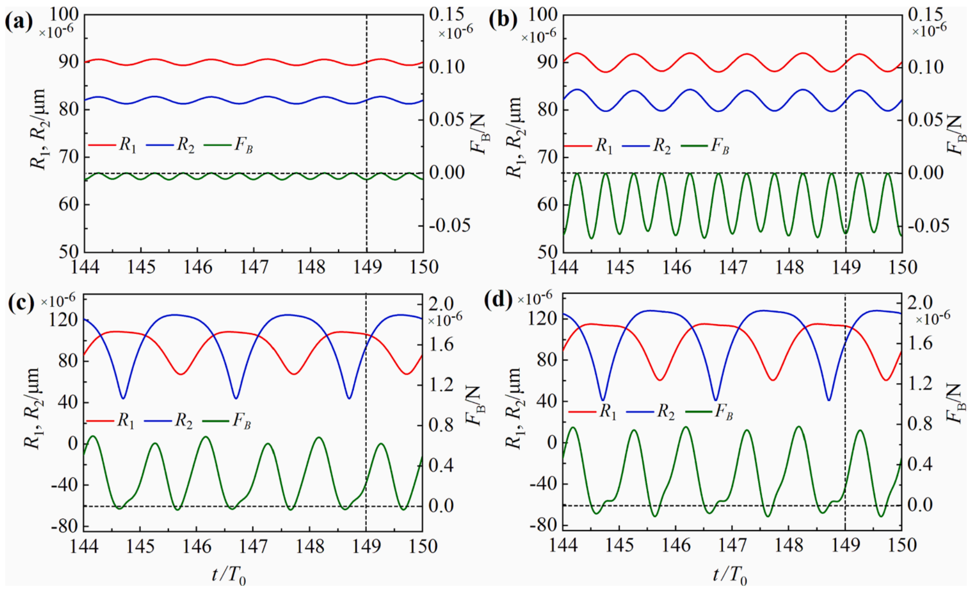

Fig. 9. Time evolution of the radial oscillations of the bubbles (R_{01} = 90 μm & R_{02} = 82 μm) and the secondary Bjerknes force F_B. **(a)** P_a = 0.1 bar, **(b)** P_a = 0.3 bar, **(c)** P_a = 0.6 bar, and **(d)** P_a = 0.9 bar. f_0 = 75 kHz and D_0 = 3500 μm.

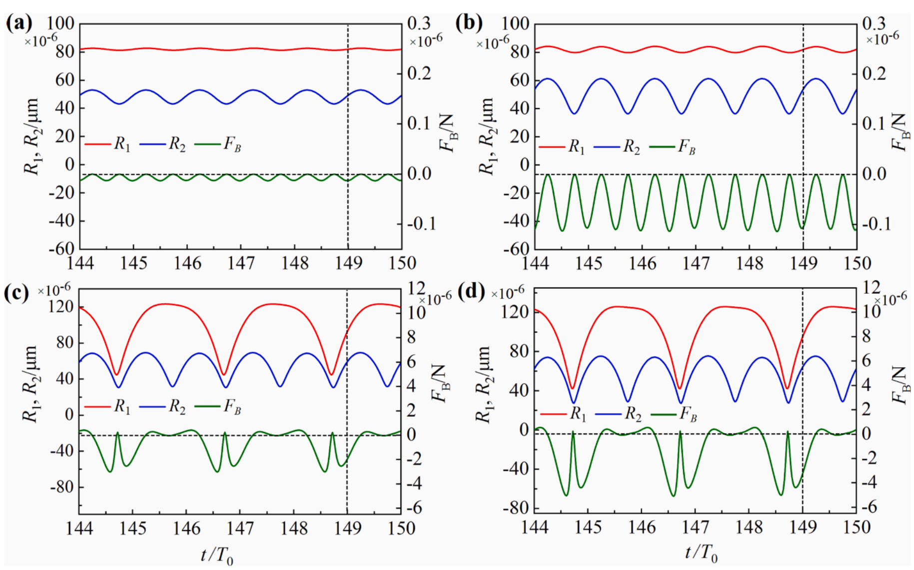

Fig. 10. Time evolution of the radial oscillations of the bubbles (R_{01} = 82 μm & R_{02} = 48 μm) and the secondary Bjerknes force F_B. P_a = **(a)** 0.1 bar, **(b)** 0.3 bar, **(c)** 0.6 bar, and **(d)** 0.9 bar. f_0 = 75 kHz and D_0 = 3500 μm.

appear. When P_a = 0.6 or 0.9 bar, the fundamental and harmonic frequency spectral lines are submerged by the raised broadband noise signals, indicating that the bubbles have possessed chaotic translational behaviors [67,68]. These analyses are consistent with the results shown in Fig. 11.

Figs. 13 and 14 present the radial motion characteristics of the bubble 1 (R_{01} = 46 μm) when the pressure amplitude P_a = 0.3 and 0.6 bar. When P_a = 0.3 bar, the period of the radial oscillation is equal to T_0 (Fig. 13(a)). The steady-state solution curve periodically repeats with f_0, and the obtained phase trajectory is a closed curve (Fig. 13(b)). There is only one point on the Poincare section (Fig. 13(c)). Only fundamental and harmonic spectral lines are in the power spectrum (Fig. 13(d)). These analyses indicate that radial motion of the bubble 1 is periodic when P_a = 0.3 bar. When P_a = 0.6 bar, bubble 1 oscillates with irregular radii and frequencies (Fig. 14(a)). The motion trajectory is an extremely dense curve that will never close (Fig. 14(b)). A sequence of points with a special fractal structure occurs in the Poincaré section (Fig. 14(c)), suggesting that this bubble is in the chaotic oscillation mode [54,69]. In addition to the spectral lines, a continuous spectrum composed by many irregular frequency components occurs (Fig. 14(d)). These analyses indicate that the radial motion of bubble 1 is chaotic when P_a = 0.6 bar [67,68].

Fig. 15 gives the bifurcation diagram of the normalized radii of bubble 1 (R_{01} = 46 μm) versus the pressure amplitude P_a. When P_a is within [0.4, 0.46 bar], bubble 1 is in a periodic oscillation state, and the chaotic oscillation can be found when P_a is within [0.46, 0.535 bar]. Different from that periodic oscillation to chaos through period-doubling bifurcation, the bubble considering the interaction force suddenly transits from periodic to chaotic state when P_a = 0.46 bar, which reflects the sensitive dependence of the system on variable parameters and is also an important feature of the binary bubble nonlinear system.

The translational motions of the bubbles are determined by the

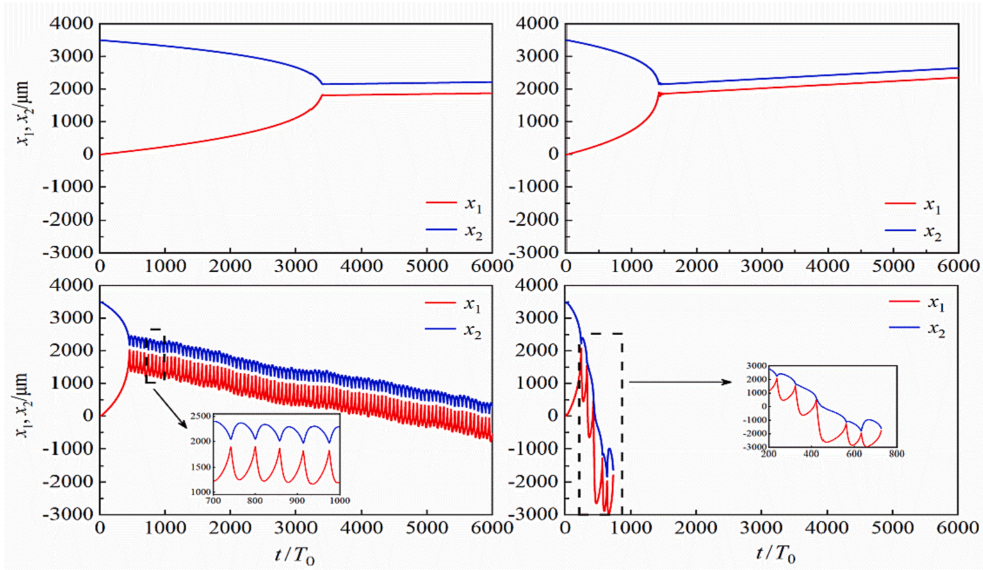

Fig. 11. Time evolution of the translational displacements of the bubbles (R_{01} = 46 μm, R_{02} = 60 μm) when **(a)** P_a = 0.1 bar, **(b)** P_a = 0.3 bar, **(c)** P_a = 0.6 bar, and **(d)** P_a = 0.9 bar. f_0 = 75 kHz, D_0 = 3500 μm.

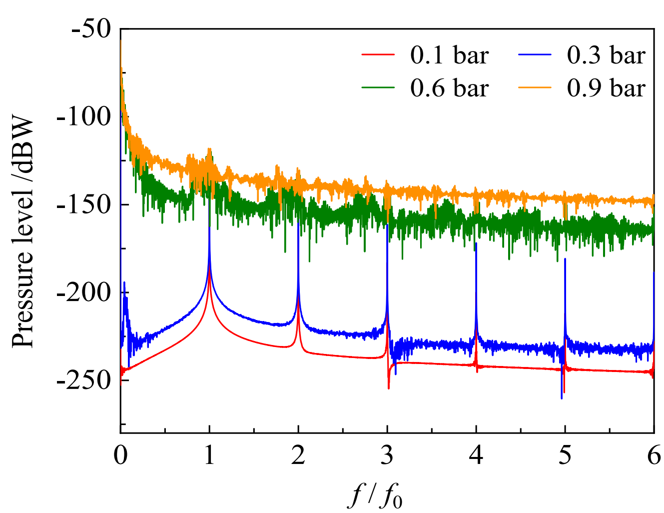

Fig. 12. Noise spectra of the time-dependent inter-bubble distance (R_{01} = 46 μm, R_{02} = 64 μm) when **(a)** P_a = 0.1 bar, **(b)** P_a = 0.3 bar, **(c)** P_a = 0.6 bar, and **(d)** P_a = 0.9 bar. f_0 = 75 kHz, D_0 = 3500 μm.

resultant force F_{h1} of the secondary Bjerknes force F_B and viscous resistance F_{ex1}. Fig. 16 gives the time-variations of the translational velocity $\dot{x}_1$ and force analysis of bubble 1 (R_{10} = 46 μm) when P_a = 0.6 bar. The direction from bubble 1 to bubble 2 is negative, while it is positive from bubble 2 to bubble 1. The chaotic pair is characterized by possessing an alternately attractive and repulsive F_B and opposite F_{ex1}, eventually leading to an alternate F_{h1} and$\dot{x}_1$.

The inter-bubble distances corresponding to the points **a**, **b**, **c** and **d** (Fig. 16 (b)) are approximately 400, 220, 240, and 520 μm. Fig. 17 gives the frequency response curves of the bubble 1 (R_{01} = 46 μm) when D is 400, 220, 240, and 520 μm. The pressure amplitude is 0.005 bar (linear condition). As shown in Fig. 17 that a bubble interacting acoustically with a neighboring bubble has two linear resonance frequencies, both of which are significantly affected by the inter-bubble distance. The left linear resonance peaks of the curves are caused by the coupling effect between the bubbles, whose value represents the linear resonance frequency of another coupled bubble. Differently, the right linear resonance peaks of the curves (plotted in the black dashed frame) are owing to the directly linear response of the bubble to the external ultrasonic driving, the evolution of which is the focus of our next work.

For convenience of the analysis, the time-dependent bubble oscillations and F_B in one driving period (**a**: 491st period; **b**: 494th period; **c**: 497th period; **d**: 500th period, marked with filled circles in Fig. 16(b)) are shown in Fig. 18. Apparently, for point **a** (D = 400 μm), the linear resonance frequency of the coupled bubble 1 $f_{c\text{-}res1}$ (=72.5 kHz) is slightly greater than f_{nat1} (=71 kHz) (Fig. 17(b)). The frequency of the sound field f (=f_0 = 75 kHz) falls on the same side of $f_{c\text{-}res1}$ (=72.5 kHz) and $f_{c\text{-}res2}$ (=50 kHz). Thus the time-averaged F_B is negative (attraction force) within one period because the in-phase radial oscillations are dominant in one driving period (Fig. 18(a)), which causes the bubble to accelerate to translate along the attraction direction under the action of F_{h1}. In this particular case, with increasing time, the $f_{c\text{-}res1}$ further increases owing to the decrease of D (D = 220 μm, point **b**), resulting in f (=75 kHz) falling within the range of $f_{c\text{-}res1}$ (=78.5 kHz) and $f_{c\text{-}res2}$ (=48.5 kHz) (Fig. 17(a)). Furthermore, there are many continuous spectral components greater or less than f_0 in the power spectrum of bubble 1 (Fig. 14(d)), indicating that the translational motion is determined by more than one time scale [34]. Eventually, these two factors combined to cause the bubble to oscillate out-of-phase (Fig. 18(b)). Correspondingly the F_B is positive (repulsive force), hence the bubble decelerates in the direction of attraction until $\dot{x}_1$ decreases to zero. After then, the bubble begins to accelerate in the direction of repulsive. When D reaches 240 μm (point **c**), f (=75 kHz) is still within the range of $f_{c\text{-}res1}$ (=76.5 kHz) and $f_{c\text{-}res2}$ (=49 kHz). Consequently, the bubbles still exhibit out-of-phase oscillations mode, and F_B is positive (Fig. 18(c)). As D increases to a certain extent (e.g. D = 520 μm, point **d**), the decrease of $f_{c\text{-}res1}$ causes f (=75 kHz) on the same side as $f_{c\text{-}res2}$ (=50 kHz) and $f_{c\text{-}res1}$ (=72 kHz) (Fig. 17(a)). Correspondingly time-averaged F_B becomes negative (Fig. 18(d)). At this time, the bubbles decelerate in the direction of repulsion until the velocity decreases to zero, and then start the subsequent alternate motions of attraction and repulsion. Based on the aforementioned analysis, we can conclude that the interaction between the bubbles can change the resonance frequencies of the coupled bubbles [10,23,47,53,70]. Thus, as the bubbles translate and proceed closer or further from one another, their net force can change and sign reversal can occur.

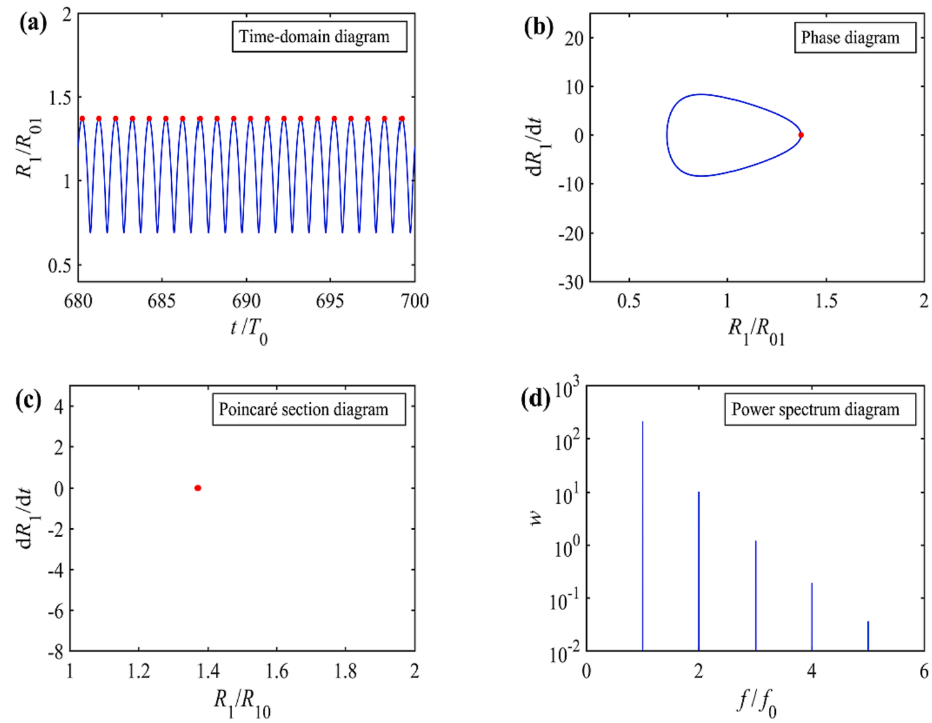

Fig. 13. Radial oscillation characteristics of bubble 1. P_a = 0.3 bar, f_0 = 75 kHz, D_0 = 3500 μm.

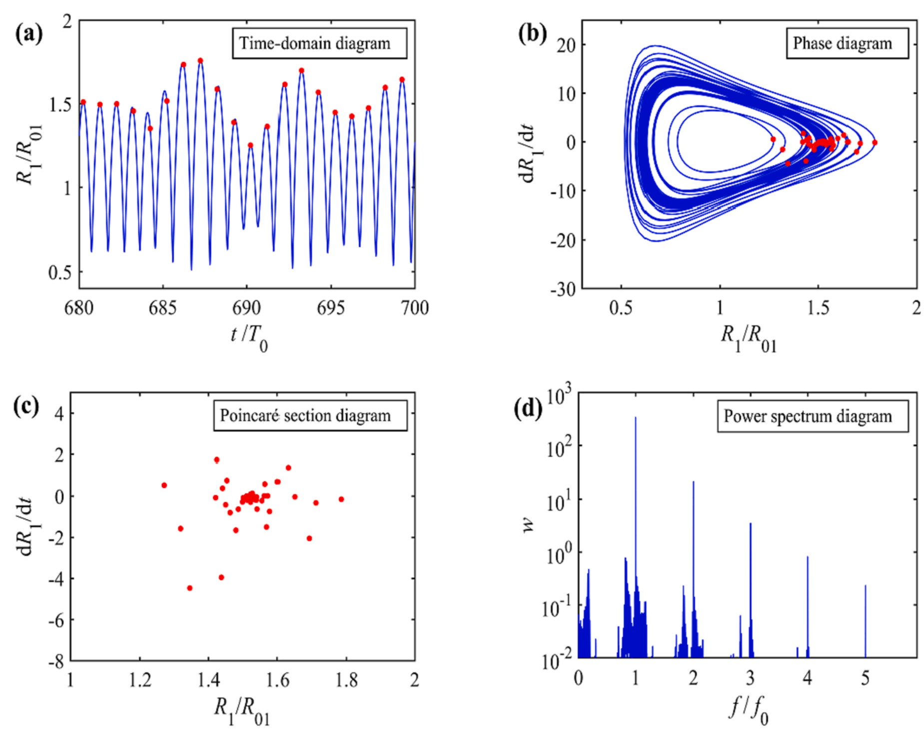

Fig. 14. Radial oscillation characteristics of bubble 1. P_a = 0.6 bar, f_0 = 75 kHz, D_0 = 3500 μm.

3.2. Influence of the initial inter-bubble distance

The initial inter-bubble distance is crucial for the secondary Bjerknes forces and dynamic characteristics of bubbles [71], which ultimately results in the changes in translational motions. Fig. 19 examines the distributions of the translational motion types in the R01-R02 plane at D_0 = 1500, 3500, 5500, and 7500 μm. The distribution ranges of the bubble pairs with an invariant D (green region) gradually increase as D_0 increases, which can be explained by the reduced translational velocities caused by the low F_B because F_B is inversely proportional to D [72]. In addition, the chaotic bubble pairs only appear when D_0 = 1500 μm (Fig. 19 (a)) owing to the stronger F_B compared to that of D_0 = 3500, 5500, or 7500 μm (Fig. 19(b, c, or d)). As D_0 increases, the distribution ranges of the coalescence pairs caused by the in-phase radial oscillations of the bubbles, and the main, 2nd order harmonic, and 1/2 order sub-harmonic, gradually decrease or disappear. These aforementioned

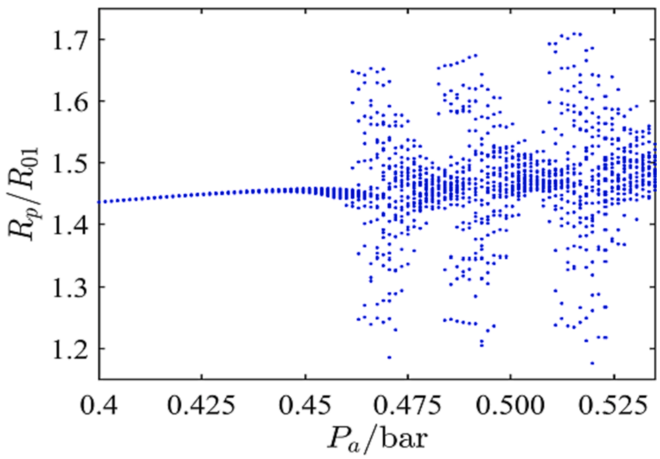

Fig. 15. Bifurcation diagrams of the normalized radii of bubble 1 (R_{01} = 46 μm) with the pressure amplitude P_a. f_0 = 75 kHz and D_0 = 3500 μm.

phenomena are mainly due to the decreased inter-bubble distances leading to the increased interaction between the two bubbles, which eventually causes the decreased pressure thresholds of the 1/2 order subharmonic resonances and chaos [10,47,53].

3.3. Influence of the driving frequency

The driving frequency is a key factor affecting the bubble radial dynamic [73]. When $P_a = 0.3$ bar and $D_0 = 3500$ μm, Fig. 20 shows the distributions of the translational motion types in the R01-R02 plane when f0 is 45, 75, 105, and 135 kHz. The corresponding R_{res} values are 75, 45, 32, and 25 μm.

The boundaries of the divided regions tend to the smaller equilibrium radii because R_{res} decreases as f_0 increases. The decrease in the distribution range of the coalescence pairs is caused by the main resonance, while the increase in its distribution range is caused by the 1/2 order subharmonic. Nevertheless, the increase caused by the 1/2 order subharmonic is unexpected, since the absorptions and scatterings of the acoustic wave in liquid are mainly caused by large bubbles with a diameter>100 μm formed by bubble aggregations [20,74]. For $f_0 = 45$ kHz (Fig. 20(a)), the transitions of the translational motions caused by

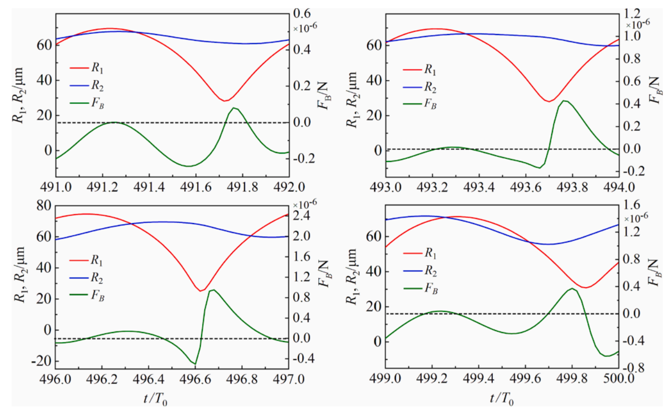

Fig. 18. Time evolution of the radial oscillations and the secondary Bjerknes force F_B. P_a = 0.6 bar, f_0 = 75 kHz and D_0 = 3500 μm.

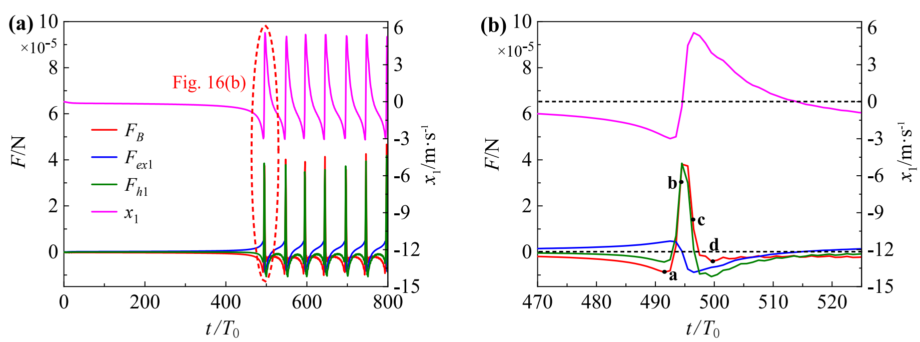

Fig. 16. **(a)** Time evolution of translational velocity $\dot{x}_1$ and force analysis of bubble 1 (R_{01} = 46 μm) when P_a = 0.6 bar. **(b)** The enlarged view in the dash line area of Fig. 16(a). f_0 = 75 kHz and D_0 = 3500 μm.

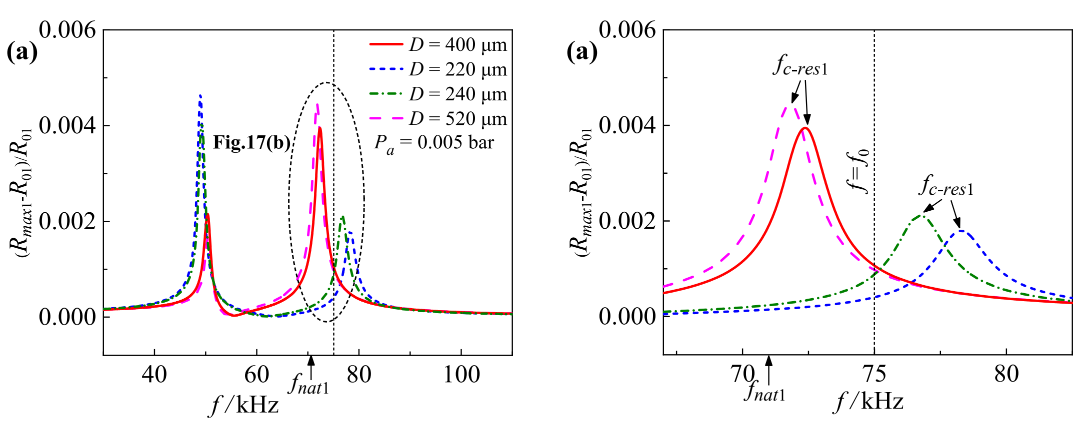

Fig. 17. **(a)** The frequency response curves of the bubble 1 (R_{01} = 46 μm) when D = 400, 220, 240, and 520 μm. **(b)** The enlarged view in the dash line area of Fig. 17(a). f_0 = 75 kHz and P_a = 0.005 bar. $f_{c\text{-}res1}$: linear resonance frequency of the coupled bubble 1 (R_{01} = 46 μm). f_{nat1} (=71 kHz): natural frequency of the individual bubble 1.

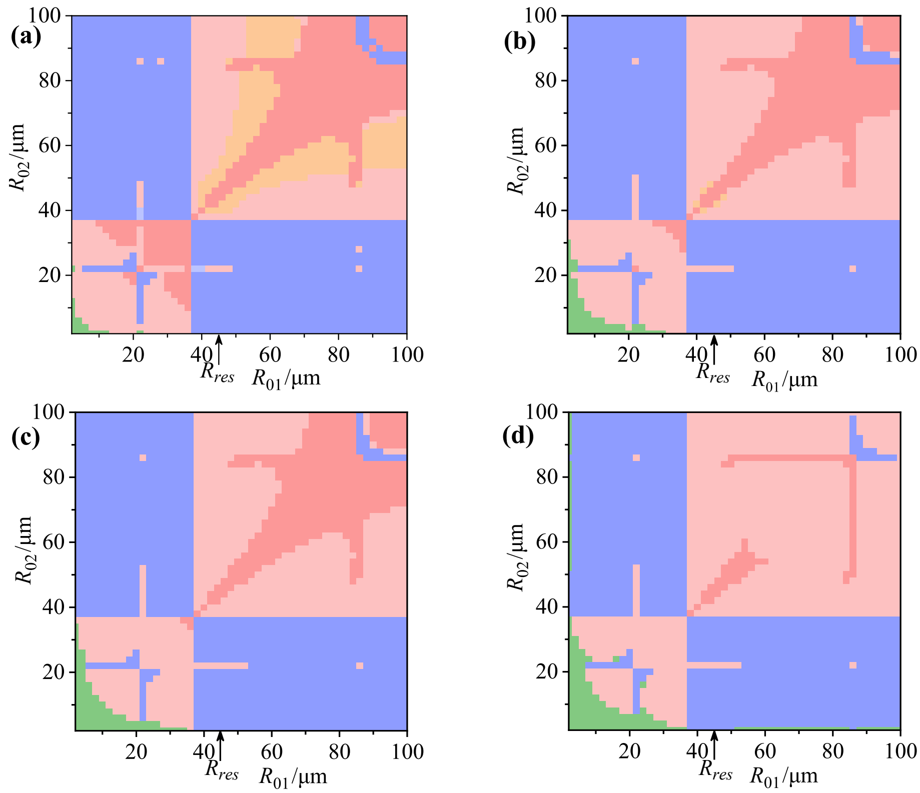

Fig. 19. The R01-R02 plane distribution diagram for six types of the translational motions. $f_0 = 75$ kHz, $P_a = 0.3$ bar. **(a)** $D_0 = 1500$ μm, **(b)** $D_0 = 3500$ μm, **(c)** $D_0 = 5500$ μm, and **(d)** $D_0 = 7500$ μm.

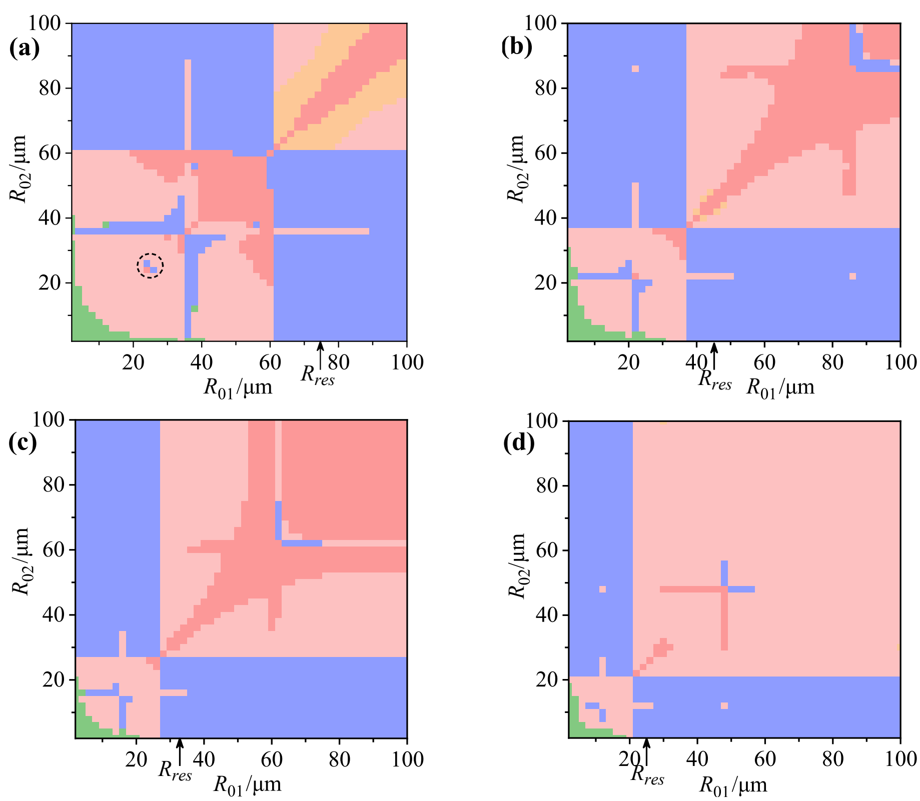

Fig. 20. The R01-R02 plane diagrams for the translation motion types at **(a)** $f_0 = 45$ kHz, **(b)** $f_0 = 75$ kHz, **(c)** $f_0 = 105$ kHz, and **(d)** $f_0 = 135$ kHz. $P_a = 0.3$ bar and $D_0 = 3500$ μm.

the 3rd order harmonic resonance (marked by black dashed circle) first appear in the R_{01}-R_{02} plane. This is because the lower driving frequency leads to more intense nonlinear radial oscillations compared with 75 kHz, 105 kHz, and 135 kHz. Notably, the chaotic pairs (yellow region) also appear in the region between the coalescence pairs and stable pairs after attraction at $R_{01} > R_{res}$ and $R_{02} > R_{res}$, as shown in Fig. 20(a).

4. Conclusions

In this study, the transition mechanisms of the translational motions of bubbles caused by the harmonic, subharmonic resonance, and chaos are studied. The influences of the driving frequency f_0 and the initial inter-bubble distance D_0 on the translational motions are also investigated.

The translational motions under the action of F_B are divided into the following: constantly repulsive pair, stable pair after repulsion, pair with invariant inter-bubble distance, stable pair after attraction, coalescence pair after attraction and chaotic pair. As P_a increases, the changes in the oscillation periods of the bubbles lead to the occurrences of harmonic or subharmonic resonances, and eventually cause the phase difference among the nonlinear radial oscillations. Therefore, the translational motions change from the previously repulsed bubbles to attractive bubbles through the action of the 2nd order harmonic wave; meanwhile, the bubbles change from an attractive, stable pair after attraction, repulsive transform to repulsive, coalescence and attractive state through the action of 1/2 order subharmonic wave. Furthermore, the linear resonance frequency of the bubble varying with the inter-bubble distance plus the effect of multi-scale time cause attractive-repulsive alternating transitions of F_B between the two bubbles. These chaotic bubble pairs, whose sizes are within the main and 1/2 order subharmonic resonance radii, usually occur in the region between the coalescence pairs and stable pairs after attraction. Finally, as D_0 increases, the distribution ranges of the bubble pairs with an invariant D gradually increase, while those of coalescence pairs decrease or disappear. With the increase of f_0, the decrease in the distribution range of the coalescence pairs is caused by the main resonance, while the increase in its distribution range is caused by the 1/2 order subharmonic. For $f_0 =$ 45 kHz, the transitions of the translational motions caused by the 3rd order harmonic first appear in the R_{01}-R_{02} plane, and the chaotic pairs also appear at $R_{01} > R_{res}$ and $R_{02} > R_{res}$.

Declaration of Competing Interest

The authors declare that they have no known competing financial interests or personal relationships that could have appeared to influence the work reported in this paper.

Data availability

Data will be made available on request.

Acknowledgments

This study was funded by the National Natural Science Foundation of China (Grant nos. 52276026, 52006136 and 11904384), Key Research Program of Frontier Sciences, CAS (No. ZDBS-LY-SLH037).

References

[1] E.A. Neppiras, Acoustic cavitation, Phys. Rep. 61 (1980) 159–251.
[2] A. Muthupandian, The characterization of acoustic cavitation bubbles-An overview, Ultrason. Sonochem. 18 (2011) 864–872.
[3] N.P. Vichare, P. Senthilkumar, V.S. Moholkar, P.R. Gogate, A.B. Pandit, Energy analysis in acoustic cavitation, Ind. Eng. Chem. Res. 39 (2000) 1480–1486.
[4] D.J. Flannigan, K.S. Suslick, Plasma formation and temperature measurement during single-bubble cavitation, Nature 434 (2005) 52–55.
[5] Y. Tao, P. Wu, Y. Dai, X. Luo, S. Manickam, D. Li, Y. Han, P.L. Show, Bridge between mass transfer behavior and properties of bubbles under two-stage ultrasound-assisted physisorption of polyphenols using macroporous resin, Chem. Eng. J 436 (2022), 135158.
[6] J. Gao, C. Li, D. Xu, P. Wu, W. Lin, X. Wang, The mechanism of ultrasonic irradiation effect on viscosity variations of heavy crude oil, Ultrason. Sonochem. 81 (2021), 105842.
[7] R. Park, M. Choi, E.H. Park, W. Shon, H. Kim, W. Kim, Comparing cleaning effects of gas and vapor bubbles in ultrasonic fields, Ultrason. Sonochem. 76 (2021), 105618.
[8] E. Dalodière, M. Virot, P. Moisy, S.I. Nikitenkoa, Effect of ultrasonic frequency on H_2O_2 sonochemical formation rate in aqueous nitric acid solutions in the presence of oxygen, Ultrason. Sonochem. 29 (2016) 198–204.
[9] A. Siddiq, E. Ghassemieh, Thermomechanical analyses of ultrasonic welding process using thermal and acoustic softening effects, Mech. Mater. 40 (2008) 982–1000.
[10] M. Guédra, C. Cornu, C. Inserra, A derivation of the stable cavitation threshold accounting for bubble-bubble interactions, Ultrason. Sonochem. 38 (2017) 168–173.
[11] V.H. Wim, D.V.S. Miguel, T.W. Lisa, F. Flemming, D.J. K, S. Kausik, W.C. E, E.J. R, Improved Sensitivity of Ultrasound-Based Subharmonic Aided Pressure Estimation Using Monodisperse Microbubbles, J. Ultras. Med. 41 (2021) 1781-1789.
[12] A. Sridharan, J.R. Eisenbrey, M. Stanczak, P. Machado, D.A. Merton, A. Wilkes, A. Sevrukov, H. Ojeda-Fournier, R.F. Mattrey, K. Wallace, F. Forsberg, Characterizing Breast Lesions Using Quantitative Parametric 3D Subharmonic Imaging: A Multicenter Study, Acad. Radiol. 27 (2020) 1065–1074.
[13] D.E. Goertz, E. Cherin, A. Needles, R. Karshafian, A.S. Brown, P.N. Burns, F. S. Foster, High frequency nonlinear B-scan imaging of microbubble contrast agents, IEEE. T. Ultrason. Ferr. 52 (2005) 65–79.
[14] M.A. O'Reilly, K. Hynynen, Blood-brain barrier: real-time feedback-controlled focused ultrasound disruption by using an acoustic emissions-based controller, Radiology 263 (2012) 96–106.
[15] K.J. Haworth, K.B. Bader, K.T. Rich, C.K. Holland, T.D. Mast, Quantitative Frequency-Domain Passive Cavitation Imaging, IEEE. T. Ultrason. Ferr. 64 (2017) 177–191.
[16] K.B. Bader, M.J. Gruber, C.K. Holland, Shaken and stirred: mechanisms of ultrasound-enhanced thrombolysis, Ultrasound, Med. Biol. 41 (2015) 187–196.
[17] L.A. Crum, Bjerknes forces on bubbles in a stationary sound field, J. Acoust. Soc. Am. 57 (1975) 1363–1370.
[18] R. Mettin, I. Akhatov, U. Parlitz, C.D. Ohl, W. Lauterborn, Bjerknes forces between small cavitation bubbles in a strong acoustic field, Phys. Rev. E 56 (1997) 2924–2931.
[19] W. Lauterborn, T. Kurz, R. Geisler, D. Schanz, O. Lindau, Acoustic cavitation, bubble dynamics and sonoluminescence, Ultrason. Sonochem. 14 (2007) 484–491.
[20] J. Lee, M. Ashokkumar, K. Yasui, T. Tuziuti, T. Kozuka, A. Towata, Y. Iida, Development and optimization of acoustic bubble structures at high frequencies, Ultrason. Sonochem. 18 (2011) 92–98.
[21] C. Wang, J. Cheng, Interaction of a bubble and a bubble cluster in an ultrasonic field, Chin. Phys. B. 22 (2013), 014304.
[22] F. Li, X. Zhang, H. Tian, J. Hu, S. Chen, R. Mo, C. Wang, J. Guo, Interactions of bubbles in acoustic Lichtenberg figure, Ultrason. Sonochem. 87 (2022), 106057.
[23] A.J. Sojahrood, Q. Li, H. Haghi, R. Karshafian, T.M. Porter, M.C. Kolios, Probing the pressure dependence of sound speed and attenuation in bubbly media: Experimental observations, a theoretical model and numerical calculations, Fluid. Dynam+. (2022).
[24] V.F.K. Bjerknes, Fields of force: a course of lectures in mathematical physics delivered December 1 to 23, Columbia University Press, New York, 1906.
[25] A. Harkin, T.J. Kaper, A. Nadim, Coupled pulsation and translation of two gas bubbles in a liquid, J. Fluid. Mech. 445 (2001) 377–411.
[26] E.A. Zabolotskaya, Interaction of gas bubbles in a sound wave field, Sov. Phys. Acoust. 30 (1984) 365–368.
[27] A.A. Doinikov, S.T. Zavtrak, On the mutual interaction of two gas bubbles in a sound field, Phys. Fluids. 7 (1995) 1923–1930.
[28] T. Barbat, N. Ashgriz, Dynamics of two interacting bubbles in an acoustic field, J. Fluid. Mech. 389 (1999) 137–168.
[29] M. Ida, A characteristic frequency of two mutually interacting gas bubbles in an acoustic field, Phys. Lett. A 297 (2002) 210–217.
[30] M. Ida, Alternative interpretation of the sign reversal of secondary Bjerknes force acting between two pulsating gas bubbles, Phys. Rev. E 67 (2003), 056617.
[31] H.N. Oguz, A. Prosperetti, A generalization of the impulse and virial theorems with an application to bubble oscillations, J. Fluid. Mech. 218 (1990) 143–162.
[32] N.A. Pelekasis, J.A. Tsamopoulos, Bjerknes forces between two bubbles. Part 2. Response to an oscillatory pressure field, J. Fluid. Mech. 254 (1993) 501–527.
[33] X. Zhang, F. Li, C. Wang, R. Mo, J. Hu, J. Guo, S. Lin, Effects of translational motion on the Bjerknes forces of bubbles activated by strong acoustic waves, Ultrasonics 126 (2022), 106809.
[34] N.A. Pelekasis, A. Gaki, A. Doinikov, J.A. Tsamopoulos, Secondary Bjerknes forces between two bubbles and the phenomenon of acoustic streamers, J. Fluid. Mech. 500 (2004) 313–347.
[35] A.A. Doinikov, Translational motion of two interacting bubbles in a strong acoustic field, Phys. Rev. E 64 (2001), 026301.
[36] A.A. Doinikov, Effects of the secondary harmonic on the secondary Bjerknes force, Phys. Rev. E 59 (1999) 3016–3020.
[37] Y. Zhang, Y. Zhang, S. Li, The secondary Bjerknes force between two gas bubbles under dual-frequency acoustic excitation, Ultrason. Sonochem. 29 (2016) 129–145.

[38] L. Zhang, W. Chen, Y. Shen, Y. Wu, G. Zhao, The nonlinear characteristics of the pulsations, translations and the secondary Bjerknes force, Chaos. Soliton. Fract. 152 (2021), 111322.
[39] L. Zhang, W. Chen, Y. Wu, Y. Shen, G. Zhao, Repulsive bubble-bubble interaction in ultrasonic field, Chin. Phys. B. 30 (2021), 104301.
[40] X. Wang, W. Chen, M. Zhou, Z. Zhang, L. Zhang, Dynamics of double bubbles under the driving of burst ultrasound, Ultrason. Sonochem. 84 (2022), 105952.
[41] K. Klapcsik, F. Hegedus, Study of non-spherical bubble oscillations under acoustic irradiation in viscous liquid, Ultrason. Sonochem. 54 (2019) 256–273.
[42] R.G. Holt, L.A. Crum, Acoustically forced oscillations of air bubbles in water: Experimental results, J. Acoust. Soc. Am. 91 (1998) 1924–1932.
[43] Y.A. Ilinskii, M.F. Hamilton, E.A. Zabolotskaya, G.D. Meegan, Influence of compressibility on bubble interaction, Innovations in nonlinear acoustics: 17th international symposium on nonlinear acoustics, (2006) 303-310.
[44] C.T. Hsiao, J.K. Choi, S. Singh, G.L. Chahine, T.A. Hay, Y.A. Ilinskii, E. A. Zabolotskaya, M.F. Hamilton, G. Sankin, F. Yuan, P. Zhong, Modelling single- and tandem-bubble dynamics between two parallel plates for biomedical applications, J. Fluid. Mech. 716 (2013) 137–170.
[45] D. Thomas, Y.A. Ilinskii, E. Zabolotskaya, M. Hamilton, Modeling time delay in clusters of interacting bubbles, 161st Meeting Acoustical Society of America 12 (2012) 045005.
[46] M.F. Hamilton, Y.A. Ilinskii, G.D. Meegan, E.A. Zabolotskaya, Interaction of bubbles in a cluster near a rigid surface, Acoustics Research Letters, Online 6 (2005) 207–213.
[47] A.J. Sojahrood, R. Earl, H. Haghi, Q. Li, T.M. Porter, M.C. Kolios, R. Karshafian, Nonlinear dynamics of acoustic bubbles excited by their pressure-dependent subharmonic resonance frequency: influence of the pressure amplitude, frequency, encapsulation and multiple bubble interactions on oversaturation and enhancement of the subharmonic signal, Nonlinear. Dynam. 103 (2021) 429–466.
[48] H.G. Flynn, C.C. Church, Erratum: transient pulsations of small gas bubbles in water, J. Aeoust. Soe. Am. 84 (1988) 985–998.
[49] A.J. Sojahrood, R. Earl, M.C. Kolios, R. Karshafian, Investigation of the 1/2 order subharmonic emissions of the period-2 oscillations of an ultrasonically excited bubble, Phys. Lett. A 384 (2020), 126446.
[50] R.G. Holt, D.F. Gaitan, Observation of Stability Boundaries in the Parameter Space of Single Bubble Sonoluminescence, Phys. Rev. Lett. 77 (1996) 3791–3794.
[51] J.B. Keller, M. Miksis, Bubble oscillations of large amplitude, J. Acoust. Soc. Am. 68 (1980) 628–633.
[52] V.G. Levich, Convective diffusion in liquids, Physicochemical Hydrodynamics, Prentice-Hall, Englewood Cliffs, NJ, 1962.
[53] F. Dzaharudin, S.A. Suslov, R. Manasseh, A. Ooi, Effects of coupling, bubble size, and spatial arrangement on chaotic dynamics of microbubble cluster in ultrasonic fields, J. Acoust. Soc. Am. 134 (2013) 3425–3434.
[54] W. Lauterborn, T. Kurz, Physics of bubble oscillations, Rep. Prog. Phys. 73 (2010), 106501.
[55] W. Lauterborn, Numerical investigation of nonlinear oscillations of gas bubbles in liquids, J. Acoust. Soc. Am. 59 (1976) 283–293.
[56] T. Segers, N.D. Jong, M. Versluis, Uniform scattering and attenuation of acoustically sorted ultrasound contrast agents: Modeling and experiments, J. Acoust. Soc. Am. 140 (2016) 2506–2517.
[57] A.J. Sojahrood, O. Falou, R. Earl, R. Karshafian, M.C. Kolios, Influence of the pressure-dependent resonance frequency on the bifurcation structure and backscattered pressure of ultrasound contrast agents: a numerical investigation, Nonlinear. Dynam. 80 (2015) 889–904.
[58] A.J. Sojahrood, D. Wegierak, H. Haghi, R. Karshfian, M.C. Kolios, A simple method to analyze the super-harmonic and ultra-harmonic behavior of the acoustically excited bubble oscillator, Ultrason. Sonochem. 54 (2019) 99–109.
[59] J. Viti, R. Mori, F. Guidi, M. Versluis, N.D. Jong, P. Tortoli, Correspondence-Nonlinear oscillations of deflating bubbles, IEEE Trans. Ultrason., Ferroelectr., Freq. Control 59(2012) 2818-2824.
[60] A.J. Sojahrood, H. Haghi, R. Karshafian, M.C. Kolios, Classification of the major nonlinear regimes of oscillations, oscillation properties, and mechanisms of wave energy dissipation in the nonlinear oscillations of coated and uncoated bubbles, Phys. Fluids 33 (2021), 016105.
[61] R. Basude, M.A. Wheatley, Generation of ultraharmonics in surfactant based ultrasound contrast agents: use and advantages, Ultrasonics 39 (2001) 437–444.
[62] R. Varga, K. Klapcsik, F. Hegedűs, Route to shrimps: Dissipation driven formation of shrimp-shaped domains, Chaos. Soliton. Fract. 130 (2020), 109424.
[63] F. Hegedűs, Topological analysis of the periodic structures in a harmonically driven bubble oscillator near Blake's critical threshold: Infinite sequence of two-sided Farey ordering trees, Phys. Lett. A 380 (2016) 1012–1022.
[64] A. Eller, H.G. Flynn, Generation of Subharmonics of Order One-Half by Bubbles in a Sound Field, J. Acoust. Soc. Am. 46 (1969) 721–727.
[65] A. Prosperetti, Nonlinear oscillations of gas bubbles in liquids: steady-state solutions, J. Acoust. Soc. Am. 56 (1974) 878–885.
[66] A.J. Sojahrood, H. Haghi, N.R. Shirazi, R. Karshafian, M.C. Kolios, On the threshold of 1/2 order subharmonic emissions in the oscillations of ultrasonically excited bubbles, Ultrasonics 112 (2021), 106363.
[67] W. Lauterborn, E. Cramer, Subharmonic Route to Chaos Observed in Acoustics, Phys. Rev. Lett. 47 (1981) 1445–1448.
[68] W. Lauterborn, Methods of chaos physics and their application to acoustic, J. Acoust. Soc. Am 84 (1988) 1975–1993.
[69] U. Parlitz, V. Englisch, C. Scheffczyk, W. Lauterborn, Bifurcation structure of bubble oscillators, J. Acoust. Soc. Am. 88 (1990) 1061–1077.
[70] V. Pandey, Asymmetricity and sign reversal of secondary Bjerknes force from strong nonlinear coupling in cavitation bubble pairs, Phys. Rev. E 99 (2019), 042209.
[71] J. Liang, G. Han, L. Fengbin, C. Darong, Investigations on dynamics of interacting cavitation bubbles in strong acoustic fields, Ultrason. Sonochem. 34 (2017) 90–97.
[72] I. Tzanakis, G.S.B. Lebon, D.G. Eskin, K.A. Pericleousc, Characterizing the cavitation development and acoustic spectrum in various liquids, Ultrason. Sonochem. 34 (2017) 651–662.
[73] B. Sohrab, J. Amin, S. Wiria, J. Okhtay, Nonlinear transitions of a spherical cavitation bubble, Chaos. Soliton. Fract. 41 (2009) 818–828.
[74] X. Wang, Z. Ning, L. Ming, C. Sun, The Investigation of Ultrasonic Energy Attenuation in Aqueous Solutions, J. Phys. Soc. Jpn. 90 (2021), 104401.